AGU PUBLICATIONS

JGR

Journal of Geophysical Research: Solid Earth

RESEARCH ARTICLE
10.1002/2016JB013801

**Key Points:**
- "Geometric" phase mixing occurs by the thinning and stretching of individual phase domains
- Formation of thin compositional layers drives increase in the spatial density of interphase boundaries, enhancing grain boundary pinning
- Ultramylonites can be generated at shear strains of 10-100 by dynamic recrystallization and geometric phase mixing of their protoliths

**Supporting Information:**
- Supporting Information S1

**Correspondence to:**
A. J. Cross,
andrew.cross@wustl.edu

**Citation:**
Cross, A. J., and P. Skemer (2017), Ultramylonite generation via phase mixing in high-strain experiments, *J. Geophys. Res. Solid Earth*, *122*, doi:10.1002/2016JB013801.

Received 29 NOV 2016
Accepted 5 FEB 2017
Accepted article online 7 FEB 2017



# Ultramylonite generation via phase mixing in high-strain experiments

**A. J. Cross**[1] **and P. Skemer**[1]

[1]Department of Earth and Planetary Sciences, Washington University in St. Louis, St Louis, Missouri, USA

**Abstract** Dynamic recrystallization and phase mixing are considered to be important processes in ductile shear zone formation, as they collectively enable a permanent transition to the strain-weakening, grain-size sensitive deformation regime. While dynamic recrystallization is well understood, the underlying physical processes and timescales required for phase mixing remain enigmatic. Here, we present results from high-strain phase mixing experiments on calcite-anhydrite composites. A poorly mixed starting material was synthesized from fine-grained calcite and anhydrite powders. Samples were deformed in the Large Volume Torsion apparatus at 500°C and shear strain rates of $5\times10^{-5}$ to $5\times10^{-4}$ $s^{-1}$, to finite shear strains of up to $\gamma=57$. Microstructural evolution is quantified through analysis of backscattered electron images and electron backscatter diffraction data. During deformation, polycrystalline domains of the individual phases are geometrically stretched and thinned, causing an increase in the spatial density of interphase boundaries. At moderate shear strains ($\gamma\geq6$), domains are so severely thinned that they become "monolayers" of only one or two grain's width and form a thin compositional layering. Monolayer formation is accompanied by a critical increase in the degree of grain boundary pinning and, consequently, grain-size reduction below the theoretical limit established by the grain-size piezometer or deformation mechanism field boundary. Ultimately, monolayers neck and disaggregate at high strains ($17<\gamma<57$) to complete the phase mixing process. This "geometric" phase mixing mechanism is consistent with observations of mylonites, where layer (i.e., foliation) formation is associated with strain localization, and layers are ultimately destroyed at the mylonite-ultramylonite transition.

## 1. Introduction

Deformation of the Earth's lithosphere is largely accommodated by the localization of strain into narrow ductile shear zones [*Ramsay*, 1980], which are considered to be an essential feature of Earth-like plate tectonics [e.g., *Vissers et al.*, 1995; *Tackley*, 1998; *Bercovici*, 2003; *Bercovici and Ricard*, 2012; *Montési*, 2013]. Strain localization is achieved through the crystal plastic deformation of rock, manifested by the progressive development of protomylonites, mylonites, and ultramylonites with increasing strain (Figure 1). Mylonitization is characterized by the reduction of grain-size, typically via dynamic recrystallization, and is also associated with the modification of crystallographic preferred orientations (CPOs) and the spatial rearrangement of different mineral phases. In protomylonites and mylonites, phases often become arranged into compositional layers (i.e., foliation) [*Passchier and Trouw*, 2005], whereas at the high-strain mylonite-ultramylonite transition, foliation is destroyed as grains of the different mineral phases become intimately mixed together (Figure 1). While protomylonites and mylonites primarily deform by grain-size insensitive creep (i.e., dislocation creep), numerous authors have proposed that the mylonite-ultramylonite transition coincides with a switch to grain-size sensitive (GSS) creep mechanisms, such as diffusion creep and/or grain boundary sliding [e.g., *Warren and Hirth*, 2006; *Skemer et al.*, 2010; *Drury et al.*, 2011; *Kilian et al.*, 2011; *Linckens et al.*, 2011; *Okudaira and Shigematsu*, 2012; *Miranda et al.*, 2016]. Such inferences are typically based on the development of a well-mixed, polymineralic network of small, equant grains with little grain boundary curvature, numerous four-grain junctions, the weakening of a preexisting CPO, and an inferred reduction in strength or increase in strain rate. A reduction in strength is critical because it indicates that ultramylonite formation causes rheological weakening through a transition to GSS creep and thereby enables strain localization associated with ductile shear zone formation.

In monomineralic rocks, a permanent transition to the strain-weakening GSS creep regime is not expected to occur because dynamic recrystallization is balanced by surface energy-driven grain growth at small grain-sizes [e.g., *de Bresser et al.*, 2001; *Austin and Evans*, 2007, 2009; *Cross et al.*, 2015; *Platt*, 2015]. In polyphase rocks, on the other hand, secondary phases inhibit grain growth by pinning grain boundaries [*Smith*, 1948;

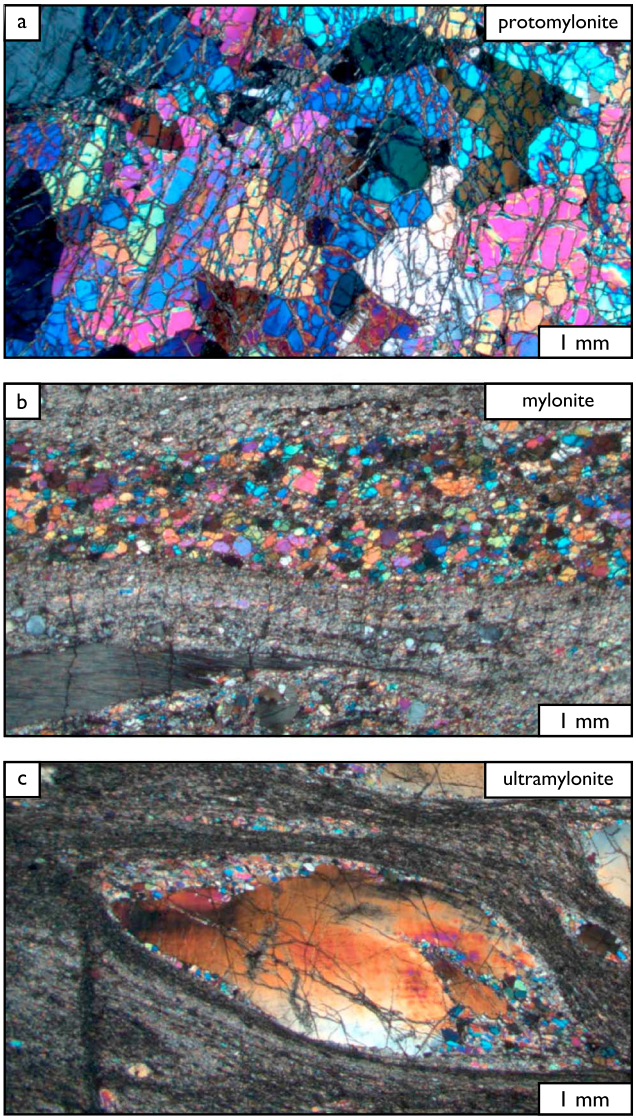


**Figure 1.** Modified after *Linckens et al.* [2015]. Photomicrographs showing textural development, with increasing shear strain, of olivine-orthopyroxene mylonites from (a) Oman and (b, c) Lanzo. With increasing shear strain, grain-size reduces dramatically by dynamic recrystallization. In the ultramylonite sample, millimeter-sized porphyroclasts are preserved within a fine-grained ($<10\ \mu m$) matrix of well-mixed olivine and orthopyroxene.

*Olgaard*, 1990; *Evans et al.*, 2001] and can therefore enable rheological weakening through a transition to GSS deformation. Furthermore, the suppression of grain growth by grain boundary pinning results in irreversible microstructural "damage," whereby grain-size remains small and ductile shear zones remain weak over long geologic timescales and repeated cycles of plate boundary activation and quiescence [*Bercovici and Ricard*, 2012]. Thus, the processes that lead to the intermixing of different mineral phases may be of critical importance to the formation and perseverance of ductile shear zones and the occurrence of Earth-like plate tectonics.

Several mechanisms have been proposed for phase mixing, many of which invoke grain boundary sliding, either through grain switching events [*Linckens et al.*, 2014], or in conjunction with subgrain rotation recrystallization [*Farla et al.*, 2013] or dissolution and precipitation [*Kilian et al.*, 2011; *Menegon et al.*, 2015; *Platt*, 2015]. Other mechanisms for phase mixing include metamorphic reactions [*Newman et al.*, 1999], melt/fluid-rock reactions [*Dijkstra et al.*, 2002; *Hidas et al.*, 2016], or heterogeneous nucleation driven by chemical [*Kruse and Stünitz*, 1999] or stress [*Kenkmann and Dresen*, 2002] gradients. For some of these mechanisms, the opening of cavities into which material can diffuse is a requisite process. Indeed, creep cavitation has been documented at middle to lower crustal conditions ($\leq$0.8 GPa), both experimentally [*Dimanov et al.*, 2007; *Rybacki et al.*, 2008] and in natural rocks [*Fusseis et al.*, 2009; *Menegon et al.*, 2015]. However, at deeper levels of the lithosphere, or under dry conditions, high effective confining pressures (nominally $>1$ GPa) will almost certainly exceed the plastic yield strength of deforming materials, thereby limiting cavity formation [*Brace and Kohlstedt*, 1980].

Despite the multitude of mechanisms proposed for phase mixing, the critical strains or timescales required to achieve well-mixed microstructures remain elusive. Previous experimental studies of phase mixing were either conducted to strains too low to observe significant changes in the degree of phase mixing, or at relatively low effective pressures, which may have aided mixing through the formation of microcracks and the diffusion of material into cavities. To elucidate the mechanisms and estimate the critical strains required for phase mixing, ultramylonite generation and strain localization in the ductile lithosphere, we present results from high-strain, high-pressure torsion experiments on initially poorly mixed calcite-anhydrite

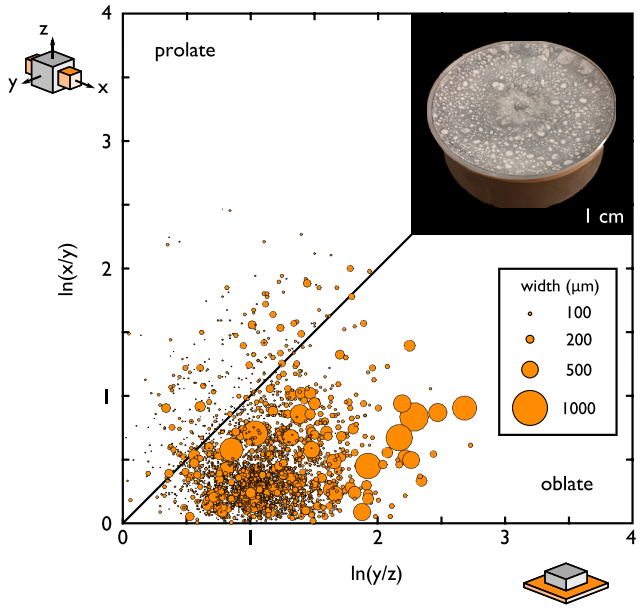


**Figure 2.** Flinn diagram showing the shapes and sizes of calcite domains in the hot-pressed calcite-anhydrite starting material, determined by fitting ellipsoids to particles imaged by micro-CT, using the BoneJ plugin [*Doube et al.*, 2010] for ImageJ. Points are sized by domain width (dimension parallel to *z*). Inset: photograph of the hot-pressed starting material. Light grey domains are pure calcite; dark grey regions are composed of both anhydrite and small calcite domains.

composites. Calcite and anhydrite are rheologically important in the upper to middle crust and can also be considered an analog for higher-pressure assemblages that have similar relative strengths. Additionally, the rheological and microstructural behavior of calcite and anhydrite is relatively well understood, thanks to numerous studies on the individual phases [e.g., *Dell'Angelo and Olgaard*, 1995; *Heidelbach et al.*, 2001; *Renner et al.*, 2002; *Herwegh et al.*, 2003; *Barnhoorn et al.*, 2004; *Hildyard et al.*, 2011] and their two-phase composites [*Bruhn and Casey*, 1997; *Bruhn et al.*, 1999; *Barnhoorn et al.*, 2005]. Previous calcite-anhydrite studies started with a well-mixed microstructure, however, and were primarily concerned with rheological contrasts rather than phase mixing—the topic of the present study.

Through analysis of our deformed samples, we show that microstructural damage results from the thinning and stretching of monophase domains, causing an increase in both the spatial density of interphase boundaries and the degree of grain boundary pinning, thereby allowing continued grain-size reduction into the GSS regime. We show that this "geometric" mechanism for phase mixing requires moderate strains for rheological weakening related to a transition to GSS creep. A simple model is described to extrapolate this phase mixing mechanism to geologic conditions. The experimental data and associated model suggest that the critical strain for ultramylonite formation is related to the ratio of the initial grain-size to the recrystallized grain-size and that large shear strains ($\gamma \leq 100$) may be required for the onset of shear localization due to phase mixing by purely mechanical means (i.e., without diffusion or reaction).

## 2. Methods

### 2.1. Starting Materials

Calcite-anhydrite composites were synthesized from fine-grained (1–3 μm), reagent-grade powders of $CaCO_3$ (calcite) and $CaSO_4$ (anhydrite). A 50–50 vol % mixture of the two powders was shaken by hand to achieve incomplete mixing of the phases. Isostatic hot pressing (HIP) of the two-phase mixture was done by Bodycote IMT Inc. (Andover, MA) at 700°C and 200 MPa confining pressure for 3 h. The final hot-pressed block contains domains of polycrystalline calcite that range widely in size (10–2000 μm in diameter), in a matrix of polycrystalline anhydrite (Figure 2; inset). X-ray microtomography (micro-CT) of a representative section of the hot-pressed block reveals that the calcite domains are mostly oblate (Figure 2): a consequence of flattening during the HIP. Starting material that was pressed isostatically at experimental conditions in the Large Volume Torsion (LVT) apparatus shows no discernible porosity (i.e., $<$ 1 vol %). Median starting grain-sizes in the matrix are 2.6 μm and 2.2 μm for calcite and anhydrite, respectively; polycrystalline calcite domains have a starting median grain-size of 3.1 μm (Table S1 in the supporting information).

Half cylinders were machined dry from the hot-pressed block using a Roland MDX-40A CNC milling machine and sectioned into a series of semicircular discs which could be put together to form disc-shaped samples (4.2 mm in diameter; 0.5 mm thick), with gold sputter coated onto the joining surface to act as a passive strain marker (Figure 3). All samples were kept in a vacuum oven at 110°C for several days before each experiment

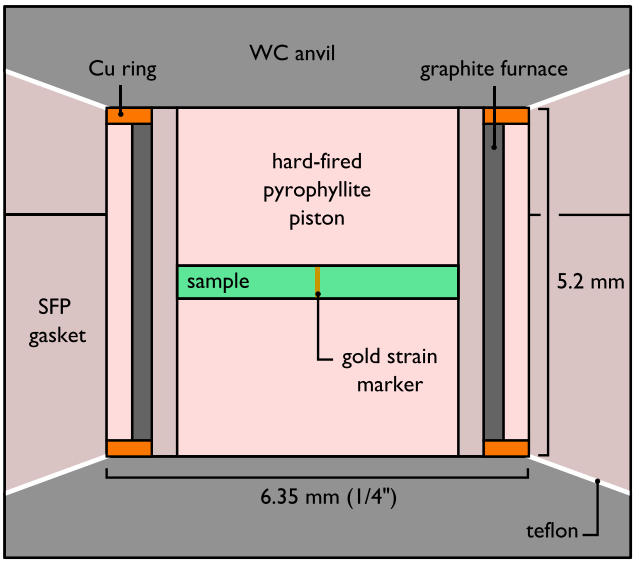


**Figure 3.** Schematic diagram of the deformation cell. A thin layer of gold is sputter coated onto each half of the sample disc (4.2 mm diameter; 0.5 mm thickness) to act as a strain marker. SFP = soft-fired pyrophyllite; WC = tungsten carbide.

to eliminate any adsorbed water. Samples cored from Carrara marble were prepared in a similar way, for comparative experiments on single-phase calcite.

### 2.2. Experimental Methods

We performed seven torsion experiments on calcite-anhydrite composites and three torsion experiments on Carrara marble in the Large Volume Torsion (LVT) apparatus at Washington University in St. Louis (Table 1). The LVT is a solid-medium, Rotational Drickamer-style apparatus in which disc-shaped samples (4.2 mm in diameter; 0.5 mm in thickness) are sheared between two opposing tungsten carbide anvils, with soft-fired pyrophyllite as the solid confining medium (Figure 3). Temperature is generated using a tubular graphite resistance furnace, held at constant power throughout the experiment. Temperature is estimated, in the absence of a thermocouple, from temperature-power relationships, calibrated from isostatic experiments with in situ thermocouples. Pressure is generated by hydraulic force, and calibrated using the Bismuth I-II transformation [*Bridgman*, 1940], assuming a linear relationship between force and pressure in the cell assembly.

Experiments were performed under constant axial load and furnace power corresponding to 1.5 GPa confining pressure and 500°C, respectively. All experiments were performed at a constant twist rate of $3.58 \times 10^{-5}$ rad/s, corresponding to a shear strain rate of $1.5 \times 10^{-4}\ s^{-1}$ at the outer radius of the sample. Some variation in the true strain rate results from thinning of the sample disc and slip along the interface between piston and anvil. Experiments were conducted to finite shear strains between 0.7 and 57, measured directly from the passive rotation of gold strain markers and verified by the relative rotation of lines drawn on the outside faces of the pistons; shear strain estimates from these two methods were often within 5% of each other.

### 2.3. Microstructural Analysis

Microstructures were analyzed on two-dimensional sections cut tangential to the deformed sample disc, corresponding to the standard reference frame (foliation perpendicular, lineation parallel). Since anhydrite

**Table 1.** Summary of Experimental Runs[a]

| Run No. | Duration (h) | Angular Shear (deg) [b] | Finite Shear Strain | Shear Strain Rate ($s^{-1}$) |
|---|---|---|---|---|
| | | *Calcite-Anhydrite HIP (50/50 Vol %)* | | |
| LVT114 | 1.78 | 35 | 0.7 | $1.1 \times 10^{-4}$ |
| LVT115 | 35.9 | 87 | 17 | $1.3 \times 10^{-4}$ |
| LVT120 | | Hydrostatic hot press | | |
| LVT124 | 19.1 | 71 | 3 | $4.4 \times 10^{-5}$ |
| LVT127 | 47.0 | 80 | 6 | $3.5 \times 10^{-5}$ |
| LVT131 | 40.8 | 89 | 57 | $3.9 \times 10^{-4}$ |
| LVT135 | 30.8 | 84 | 10 | $9.0 \times 10^{-5}$ |
| | | *Carrara Marble* | | |
| LVT128 | 40.8 | 74 | 3.5 | $5.4 \times 10^{-5}$ |
| LVT133 | 41.3 | 81 | 7 | $4.8 \times 10^{-5}$ |
| LVT136 | 1.8 | 61 | 1.8 | $2.8 \times 10^{-4}$ |

[a] All experiments were performed at 500°C and a confining pressure of 1.5 GPa.
[b] Measured on sections cut tangential to the deformed sample disc.

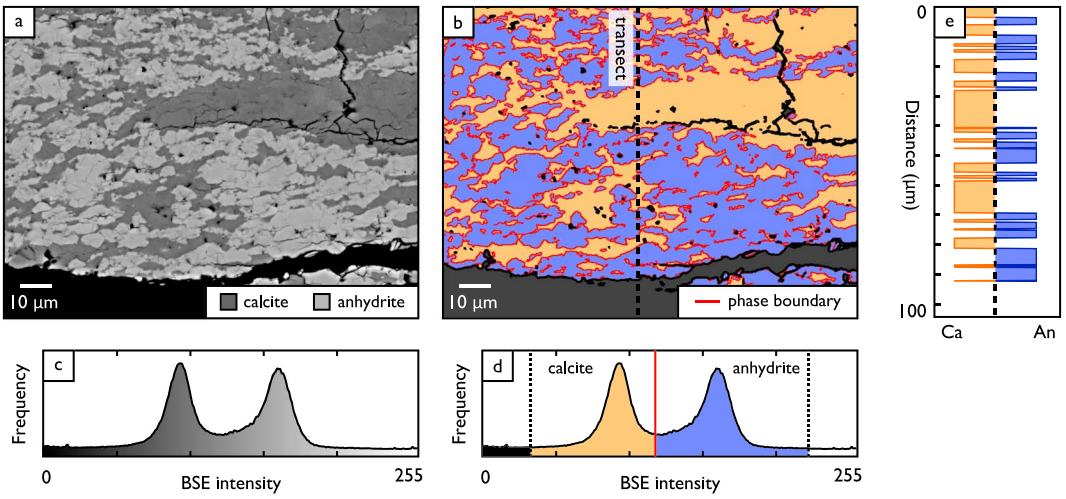


**Figure 4.** Thresholding of BSE images for the purpose of quantifying phase boundary density and domain width. (a) A BSE image is separated into (b) a phase map of calcite (low BSE intensity) and anhydrite (high BSE intensity), by thresholding of the (c, d) bimodal BSE intensity histogram. (e) Profiles drawn across the thresholded BSE image (dashed line in Figure 4b) are used to quantify calcite domain widths.

($CaSO_4$) transforms to gypsum ($CaSO_4 \cdot 2H_2O$) with the addition of water, sample sections were polished anhydrously using a combination of ethanol and grit paper (down to 600 grit), followed by a blend of polyglycol and alumina suspension powder (grit sizes of 9, 4, 1, 0.3, and 0.05 μm) on soft polishing cloths, in a procedure similar to that outlined by *Hildyard et al*. [2009]. A final stage of chemomechanical polishing using colloidal silica was avoided, since the water-based solution reacted severely with anhydrite in the samples, even under very short polishing times, generating significant surface topography and rendering the samples unsuitable for analysis.

Samples were analyzed on a JEOL 7001-LVF FE-SEM operating at an accelerating voltage of 20 kV and a beam current of 14 nA, under high vacuum conditions. Each sample was carbon coated to prevent charging. Electron backscatter diffraction (EBSD) data were collected by rastering the electron beam with a 500 nm step size. While calcite EBSD patterns were of a high quality, anhydrite proved difficult to index despite reasonable quality patterns. The raw EBSD pixel data were cleaned using the pixel-interpolation toolbox EBSDinterp (v.1.0) [*Pearce*, 2015], applying band contrast masking to improve the robustness of the interpolation. EBSD data were thereafter processed in the MTEX toolbox for MATLAB (v.4.3.2) [*Bachmann et al*., 2010].

### 2.4. Quantifying Textural and Microstructural Evolution

To quantify microstructural evolution and phase mixing, we calculate four key parameters that reflect changes in the spatial distribution of the two phases and grain-size evolution: (1) phase boundary density, (2) domain width, (3) grain-size, and (4) phase boundary fraction, outlined below. All microstructural quantification was performed on regions close to the centers of the sample sections, to avoid boundary effects.

#### 2.4.1. Phase Boundary Density

Phase boundary density is defined as the total length of phase boundaries (boundaries between grains of different phases) in a given area. Here phase boundary density is calculated from backscatter electron (BSE) images that are subjected to a thresholding algorithm in MATLAB. The thresholding method yields a straightforward discrimination of calcite and anhydrite, which have markedly different BSE intensities (Figure 4a). For each sample, five to seven BSE images are thresholded by finding the central minima of the bimodal BSE intensity distribution (Figures 4a–4d). Regions of BSE intensity above and below the threshold value belong to anhydrite and calcite, respectively. Areas of very low BSE intensity generally correspond to holes, decompression cracks, and boundaries between grains of the same phase and are excluded from the analysis. Phase boundaries, drawn between regions of high and low BSE intensity, are then used to calculate the phase boundary density, $\delta$, as follows:

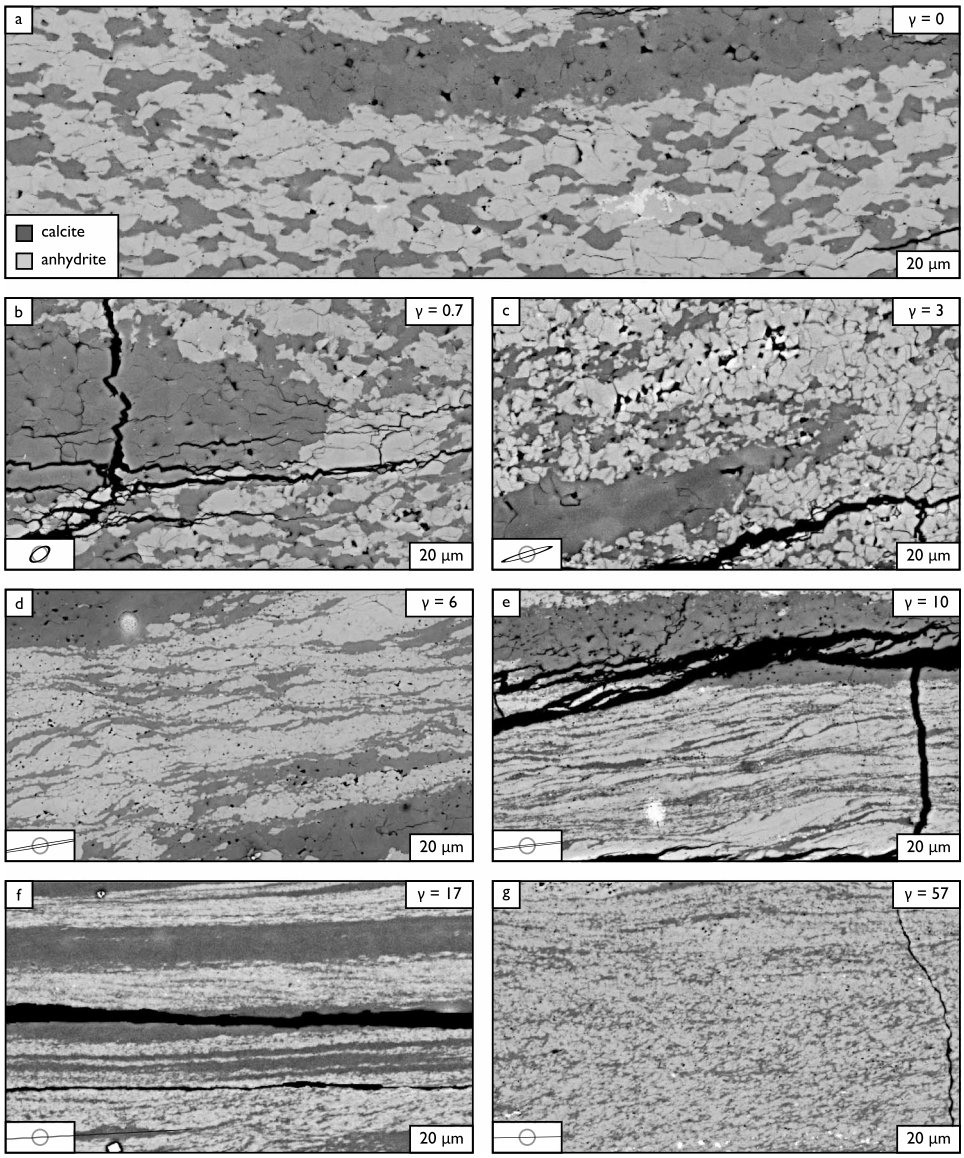


**Figure 5.** (a–g) BSE images of representative areas of the undeformed and deformed calcite-anhydrite samples. Shear sense in all images is top to the right (dextral). Regions of low BSE intensity are decompression cracks and holes formed by the plucking of grains during polishing.

$$\delta = L_{pb}/A \quad (1)$$

where $L_{pb}$ is the total phase boundary length (m) and $A$ is the area of the BSE image ($m^2$). Phase boundary density, $\delta$, has units of $m/m^2$ and is assumed to increase with progressive phase mixing. It should be noted that $\delta$ is highly sensitive to the effective resolution of the BSE images used; all values given herein are calculated from images of 400X magnification, yielding a minimum effective resolution (i.e., pixel width) of ~1 μm.

#### 2.4.2. Domain Width

With increasing deformation, the size and shape of individual calcite domains are expected to evolve. To quantify this effect, the widths of calcite domains are calculated through a similar BSE thresholding method to that outlined above. Here "width" corresponds to the calcite domain dimension normal to the shear plane (i.e., the vertical axis in BSE images shown herein). On each of the thresholded BSE images described above, 20 profiles are constructed perpendicular to the shear plane (Figures 4b and 4e) to capture a representative and

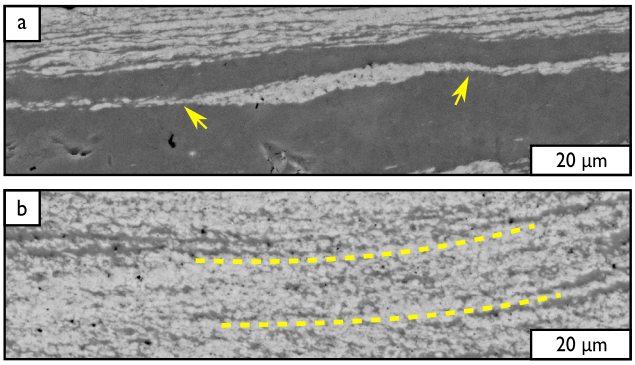


**Figure 6.** High-magnification BSE images of the two highest strain samples, (a) LVT115 ($\gamma = 17$) and (b) LVT131 ($\gamma = 57$). Domains of both anhydrite (yellow arrows) and calcite (yellow dashed lines) are (Figure 6a) thinned to monolayers (layers of one grain's width) and (Figure 6b) disaggregate with increasing deformation.

statistically robust number of domains. From these profiles, we measure calcite domain widths, ignoring spurious peaks of less than two pixels' width that are typically caused by changes in BSE intensity at grain boundaries.

#### 2.4.3. Grain-Size

We determine grain-size from EBSD analyses of our undeformed and deformed samples. For calcite, which indexed at a high rate, grains are constructed in MTEX using a 10° critical misorientation angle, without extrapolating the grains to fill non-indexed (i.e., anhydrite) regions. Grain-size is given as the diameter of an area-equivalent circle, without a stereological correction. It is important to note that grain-sizes in the highest strain samples are close to the spatial resolution of our EBSD analyses (~1 μm), limiting our ability to resolve the smallest grains in these samples (supporting information Figure S2).

For anhydrite, which produced reasonable EBSD patterns but did not index, grain-sizes (also given as area-equivalent circle diameters) were determined in ImageJ, via image analysis of band contrast maps of the non-indexed regions.

#### 2.4.4. Phase Boundary Fraction

It is anticipated that grains surrounded by a different phase are systematically smaller than those surrounded by grains of the same phase, due to grain boundary pinning effects that inhibit grain growth in polyphase composites [*Smith*, 1948; *Olgaard*, 1990; *Evans et al*., 2001]. To explore this effect, we calculate, using EBSD, the phase boundary fraction of each grain, defined as follows:

$$P_{pb} = L_{pb}/L_{total} \quad (2)$$

where for each grain, $L_{total}$ is the boundary length (i.e., the perimeter) and $L_{pb}$ is the length of phase boundary (see supporting information Figure S1). Phase boundary fraction (hereafter denoted $P_{pb}$) varies from 0, for a grain surrounded entirely by grains of the same phase, to 1, for a grain surrounded entirely by grains of a different phase. Note that while phase boundary density reflects the degree of bulk phase mixing, phase boundary fraction reflects only the local (i.e., grain scale) degree of mixing, which is useful for discriminating between grains in well-mixed and poorly mixed regions. Nevertheless, these are related quantities: phase boundary density is a function of both the phase boundary fraction and the grain-size.

## 3. Results

BSE images of undeformed and deformed samples show a significant textural evolution during deformation to large shear strains (Figure 5). In the undeformed material, polycrystalline calcite domains, which are slightly flattened from the HIP process and have a broad range of sizes (10–2000 μm), are contained within a matrix of polycrystalline anhydrite (Figure 5a). At a shear strain of 3 or more, the larger calcite domains become conspicuously thinned and stretched out. Domains at this strain are roughly elliptical, with long axes that are aligned with the long axis of the finite strain ellipse (Figures 5c–5f). Smaller calcite domains also thin and stretch out, and at a shear strain of ~6 develop a wavy, layered texture similar in appearance to S-C′ textures observed in natural mylonites (Figures 5d and 5e) [*Passchier and Trouw*, 2005]. As deformation progresses, domains of the two phases approach a thickness of only one grain width (Figure 6a), hereafter referred to as "monolayers," although, even at a shear strain of 17, several large calcite domains are still preserved. Ultimately, monolayers neck and separate into small clusters of grains, or individual grains (Figure 6), marking a local completion of phase mixing. At a shear strain of 57, monolayers are mostly obliterated and replaced with a fully mixed microstructure where calcite and anhydrite are uniformly distributed (Figures 5g and 6b) in a manner similar to that of natural ultramylonites (e.g., Figure 1c). In contrast to

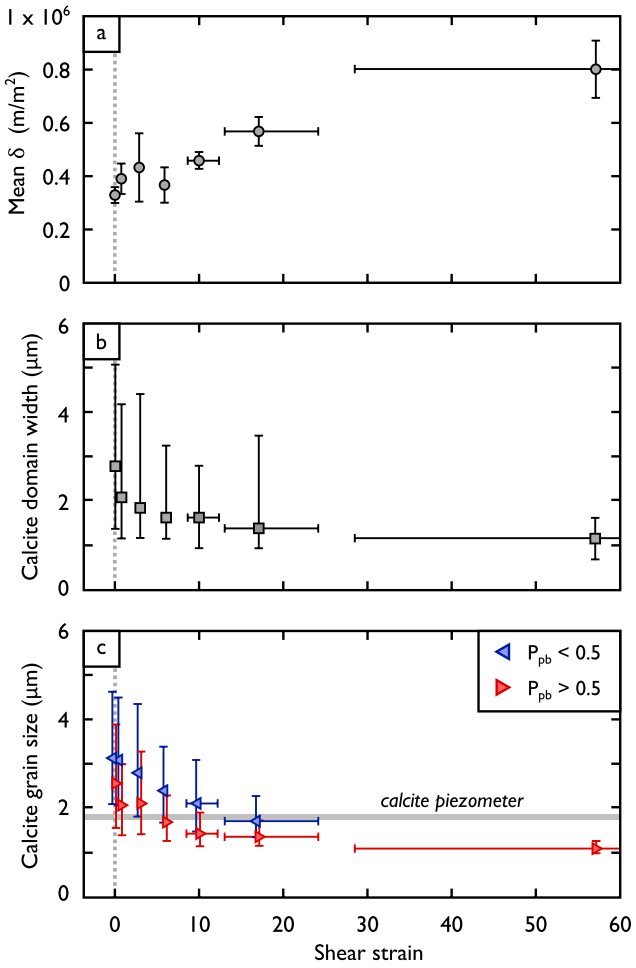


**Figure 7.** Changes in (a) mean phase boundary density, $\delta$, (b) median domain width, and (c) median calcite grain-size as a function of shear strain. Vertical bars represent the data range, given as 1 standard deviation ($1\sigma$) in Figure 7a and the 25th and 75th percentiles in Figures 7b and 7c. Horizontal bars represent the error in shear strain measurements, assuming a ±1° error in the determination of angular shear from the deflected strain marker. At low strains, this error is smaller than the size of the data points. Data can be found in the supporting information (Table S1). The calcite piezometer shown in Figure 7c is derived from Carrara marble experiments (Table 1) conducted at the same experimental conditions as the two-phase experiments.

*Barnhoorn et al.* [2005], who document a heterogeneous distribution of deformation in calcite-anhydrite composites at shear strains as low as 1, deformation in our samples was remarkably homogeneous, aside from small decreases in shear strain toward the top and bottom edges of some samples.

The textural changes outlined above (progressive phase mixing and the thinning and stretching of domains) are corroborated by microstructural quantification (Figure 7). Phase boundary density more than doubles during deformation to a shear strain of 57 (Figure 7a), while median domain widths decrease systematically by a factor of 2–3 (Figure 7b), although the range of domain widths (vertical bars on Figure 7b) is not significantly modified until the highest strain reached, signifying that large calcite domains are retained to high strains.

Meanwhile, we observe progressive grain-size reduction of both calcite and anhydrite, from a starting median grain-size of ~3 μm in the undeformed material. During deformation, grains in well-mixed regions appear systematically smaller than those in poorly-mixed regions or single-phase domains. To demonstrate this, Figure 8 shows $P_{pb}$ values for calcite in a representative area of our lowest-strain sample (LVT114; $\gamma = 0.7$). Grains with low $P_{pb}$ values (blue grains in Figure 8b) are those which reside in the interiors of calcite domains, while those with high $P_{pb}$ values (red grains in Figure 8b) are either isolated grains or grains along the edges of polycrystalline calcite domains. Both populations of grains have lognormal grain-size distributions (supporting information Figure S2). Importantly, grains with lower $P_{pb}$ values ($<0.5$) are distinctly larger than those with high $P_{pb}$ values ($>0.5$): a trend which is consistent across all our samples (Figure 7c). Furthermore, at moderate to high shear strains ($\gamma \geq 6$), grain-sizes within calcite domains ($P_{pb} < 0.5$) converge onto the calcite grain-size piezometer (Figure 7c), determined here from experiments on pure Carrara marble conducted at identical deformation conditions (Table 1). In contrast, calcite grains in well-mixed regions ($P_{pb} > 0.5$) fall below the calcite piezometer by as much as a factor of 2 in the highest strain sample.

## 4. Discussion

### 4.1. Geometric Phase Mixing Mechanism

Microstructural analyses of our deformed samples reveal a progressive increase in the degree of phase mixing and concurrent grain-size reduction with increasing shear strain. As polycrystalline domains of

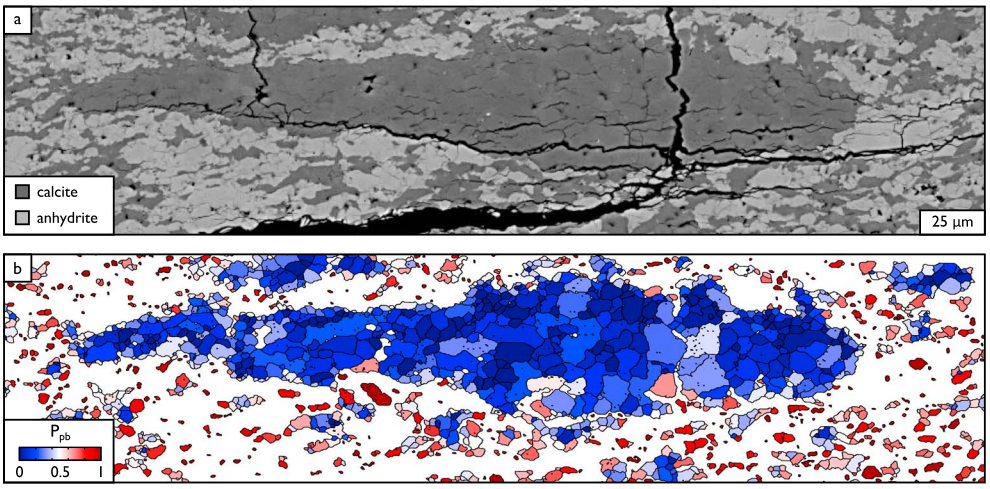


**Figure 8.** (a) Calcite EBSD data corresponding to the BSE image, from sample LVT114, deformed to $\gamma = 0.7$. (b) Grains colored by their phase boundary fraction, $P_{pb}$. Red grains are calcite grains surrounded predominately by anhydrite ($P_{pb} > 0.5$); blue grains are calcite grains surrounded predominantly by other calcite grains ($P_{pb} < 0.5$). Grains with high phase boundary fractions are systematically smaller than grains with low phase boundary fractions.

calcite and anhydrite are sheared, they thin to become monolayers of only one grain's width, causing a geometrically-driven increase in the spatial density of phase boundaries. Further deformation causes monolayers to neck and disaggregate into individual grains, resulting in a local maximization of phase boundary density. At the maximum shear strain achieved in our experiments ($\gamma = 57$), monolayers have been almost completely destroyed, and phase boundary density reaches its maximum theoretical value ($P_{pb} = 0.8 \times 10^6$ m/m$^2$; supporting information Figure S3b). We interpret these observations as evidence that phase mixing is complete.

Textural evolution in these samples can be characterized by the creation and subsequent destruction of compositional layering. The development of layers (i.e., foliation) during polyphase deformation has previously been suggested as a favorable condition for strain localization in mylonites, as it allows for the formation of an interconnected network of the weakest phase, into which deformation can localize [*Handy*, 1990; *Montési*, 2013]. Furthermore, polyphase composites with high phase boundary densities may be weaker than their individual constituent phases, because boundary diffusion rates (i.e., Coble creep or pressure solution) in polyphase composites are governed by the fastest diffusing species, whereas boundary diffusion is rate limited by the slowest diffusing species in single-phase aggregates [*Chen*, 1982; *Wheeler*, 1992; *Sundberg and Cooper*, 2008]. In fact, diffusion creep cannot proceed in a single-phase aggregate if one species is immobile, whereas polyphase composites can continue to deform by phase transformations across boundaries sweeping through immobile species [*Wheeler*, 1992]. In axial compression experiments on calcite and anhydrite, *Bruhn et al*. [1999] found that the relative weakness of their two-phase composites could not be entirely explained by variations in grain-size. They found that strength variations were correlated with the density of phase boundaries and inferred additional weakening due to enhanced diffusion along phase boundaries. Thus, the formation of monolayers (and therefore long, interconnected diffusion pathways) through the processes observed here may aid rheological weakening and strain localization beyond the predictions of a simple two-phase rheological mixing model.

### 4.2. Transition to Grain-Size Sensitive Deformation

In single-phase materials, it is hypothesized that grain-size evolution is controlled by the competing processes of dynamic recrystallization and grain growth [e.g., *de Bresser et al*., 2001], preventing a transition to GSS-dominated deformation involving diffusion creep or grain boundary sliding. However, with the addition of a secondary phase, grain growth is suppressed by grain boundary pinning [*Smith*, 1948; *Olgaard*, 1990; *Evans et al*., 2001] and may enable a permanent transition to GSS-dominated deformation, allowing significant rheological weakening and strain localization. Furthermore, the suppression of grain growth causes microstructural damage (i.e., irrecoverable grain-size reduction), resulting in long-lived

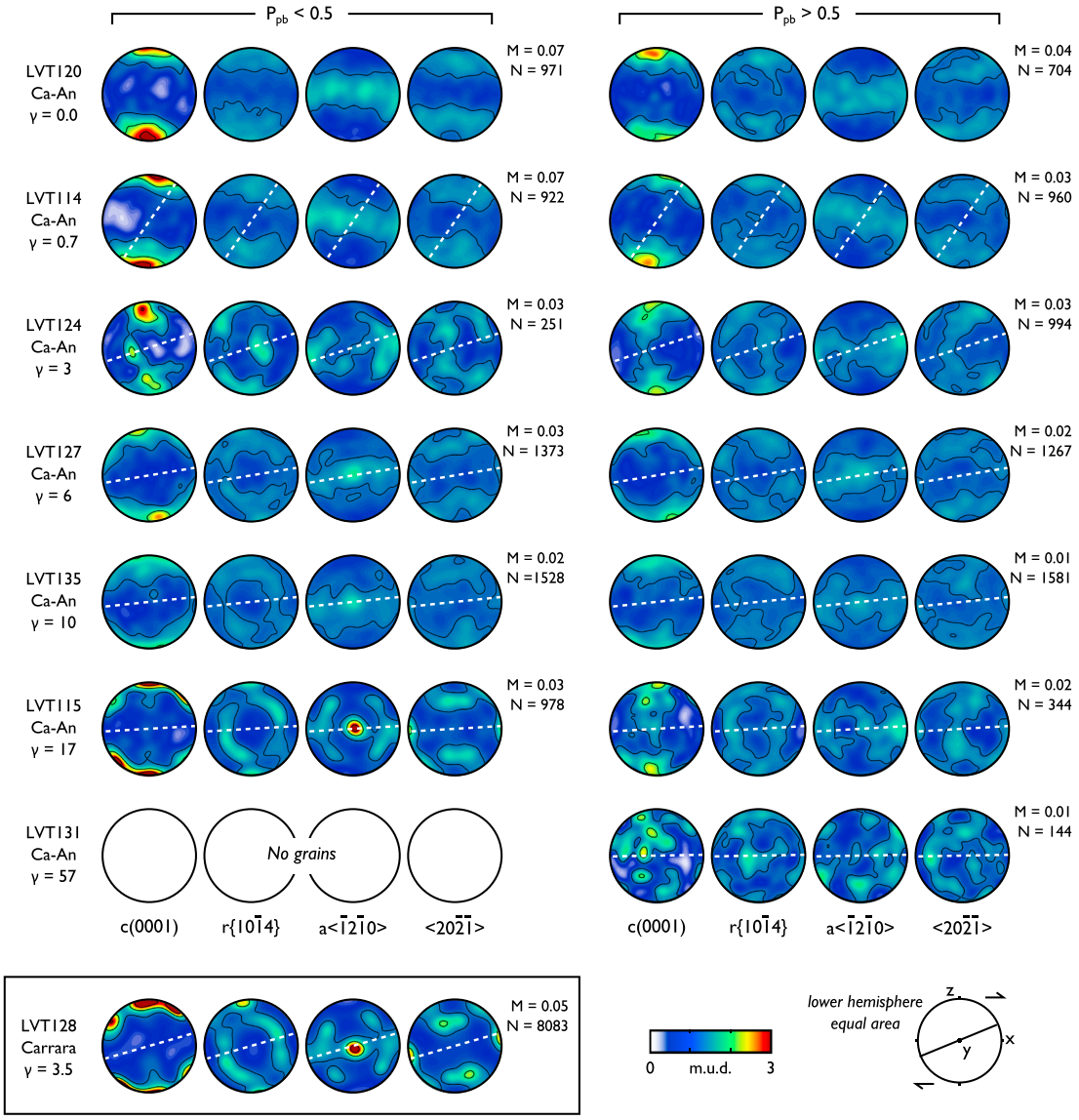


**Figure 9.** Lower hemisphere, equal area pole figures for calcite, contoured using a 10° cone half width from one-point-per-grain data (*N* grains in each sample, split into populations of $P_{pb} > 0.5$ and $P_{pb} < 0.5$). Fabric strength is given by the *M* index of *Skemer et al*. [2005]. For reference, pole figures from one experiment on single-phase calcite (Carrara marble) are included (inset). Dashed lines on pole figures represent the long axis of the finite strain ellipse.

weak rheologies that appear to characterize plate boundary shear zones [*Bercovici and Ricard*, 2012]. Three proposed signatures of a transition of GSS creep are as follows: (1) randomization of a preexisting CPO, (2) reduction of grain-size below the recrystallized grain-size piezometer, and (3) rheological weakening manifested as either a decrease in flow stress or an increase in strain rate.

#### 4.2.1. CPO Randomization

Several studies have suggested that GSS deformation mechanisms can cause the weakening and ultimate randomization of a preexisting CPO. In particular, grain rotations during grain boundary sliding may be responsible for the dispersion of crystallographic alignments [e.g., *Zhang et al*., 1994; *Bestmann and Prior*, 2003; *Skemer and Karato*, 2008; *Wheeler*, 2009] observed in many natural ultramylonites. The interpretation of calcite CPOs in our experiments is complicated by a preexisting CPO in the calcite-anhydrite starting material, imparted by the hot-pressing process, which has grains favorably oriented for $c\langle 0001\rangle\langle\bar{1}2\bar{1}0\rangle$ slip (Figure 9). With progressive deformation, components of $r^{+}\{10\bar{1}4\}\langle\bar{2}021\rangle$ and $r^{-}\{10\bar{1}4\}\langle 20\bar{2}\bar{1}\rangle$ slip

appear, generating additional *c* axis maxima on either side of the sample reference frame *z* axis (pole to shear plane). This CPO is identical to that observed in Carrara marble deformed under the same conditions in this study (supporting information Figure S4) and in previous studies [*Barnhoorn et al*., 2004].

*M* index values [*Skemer et al*., 2005] show progressive CPO weakening with increasing shear strain. Moreover, calcite grains surrounded predominately by anhydrite ($P_{pb} > 0.5$) have systematically weaker CPOs than calcite grains surrounded predominately by other calcite grains ($P_{pb} < 0.5$). In addition, the CPOs of both grain populations become weaker than CPOs developed in Carrara marble under the same conditions, above a shear strain of ~3 (Figure 9). It is possible that $P_{pb} > 0.5$ grains, which are smaller than $P_{pb} < 0.5$ grains, are deforming by a higher proportion of GSS creep and therefore experience more pronounced fabric weakening. A similar grain-size control on fabric strength was also recently interpreted by *Rahl and Skemer* [2016] as evidence of different fractional contributions from dislocation creep and GSS creep in a natural quartz mylonite.

#### 4.2.2. Overstepping of Piezometer

For many minerals—including calcite—the recrystallized grain-size piezometer approximates the mechanism boundary between dislocation creep and GSS creep [see *Austin and Evans*, 2009, Figure 1]. Consequently, a reduction in grain-size below the piezometer at a given stress will likely coincide with a transition into the GSS-dominated deformation regime [*de Bresser et al*., 2001]. In a microstructural study of gabbroic mylonites, *Mehl and Hirth* [2008] found that in mixed plagioclase-pyroxene layers, the recrystallized grain-sizes of plagioclase converged on a "polyphase piezometer," yielding smaller grain-sizes than the single-phase plagioclase piezometer at the same stresses. Furthermore, by plotting the polyphase piezometer on a deformation mechanism map, polyphase samples were placed either in the diffusion creep field or field boundary region, in contrast to single-phase layers in which plagioclase placed exclusively within the dislocation creep field. Similarly, in a study of exhumed mantle shear zones, *Linckens et al*. [2015] found olivine grain-sizes to be systematically smaller in the presence of secondary phases. *Bercovici and Ricard* [2016] recently proposed a theoretical basis for the occurrence of a secondary piezometer for polyphase rocks, which they attribute to an energy hysteresis related to polyphase "interface damage" (note that an increase in interface damage described by Bercovici and Ricard is equivalent to an increase in "phase boundary density" described in this study). Put simply, the mixing of different phases drives grains to smaller sizes than in single-phase systems, due to the effects of grain boundary pinning. Indeed, our microstructural analyses (Figure 7c) show that calcite grains in essentially single-phase regions ($P_{pb} < 0.5$) converge onto the calcite piezometer, while calcite grains surrounded predominately by anhydrite ($P_{pb} > 0.5$)—including calcite grains within monolayers—are pushed below the calcite piezometer above a shear strain of ~6. In fact, the depression of grain-sizes below the calcite piezometer is likely underrepresented by our data, due to a truncation of the grain-size histograms related to the EBSD spatial resolution, as mentioned above. Indeed, grains in the most well-mixed regions of the highest strain samples appear considerably smaller than 500 nm (Figure 6).

#### 4.2.3. Rheological Weakening

A grain-size modulated transition from dislocation to diffusion creep has been widely proposed as a mechanism by which rheological weakening can occur. In many monophase materials, only small strains can be accumulated by diffusion creep because grain growth increases diffusion length scales and promotes dislocation creep [*Pearce and Wheeler*, 2011]. In contrast, the suppression of grain growth in well-mixed polyphase composites can enable long-lived rheological weakness. Persistent weak zones in the lithosphere that can be reactivated throughout the cycle of plate formation and destruction are likely essential for Earth-like plate tectonics [*Bercovici and Ricard*, 2012].

Although the LVT apparatus does not directly measure flow stress, we can estimate stress indirectly using empirical flow laws. Figure 10 shows deformation mechanism maps for calcite and anhydrite, calculated using the dislocation creep, grain boundary sliding, and diffusion creep flow laws of *Renner et al*. [2002], *Walker et al*. [1990], and *Herwegh et al*. [2003], respectively, for calcite and the dislocation and diffusion creep flow laws of *Dell'Angelo and Olgaard* [1995] for synthetic (HIP) anhydrite. At the conditions of our experiments, the calcite piezometers of *Rutter* [1995] and *Barnhoorn et al*. [2004] and the paleowattmeter of *Austin and Evans* [2007, 2009] all closely coincide with the calcite deformation mechanism field boundary (Figure 10a). Moreover, data points corresponding to calcite grains with $P_{pb} < 0.5$ plot close to these relationships, within the field boundary region, while data points for grains with $P_{pb} > 0.5$ typically plot below the field boundary region, especially at $\gamma \geq 6$. Importantly, this transition coincides with the strain at which

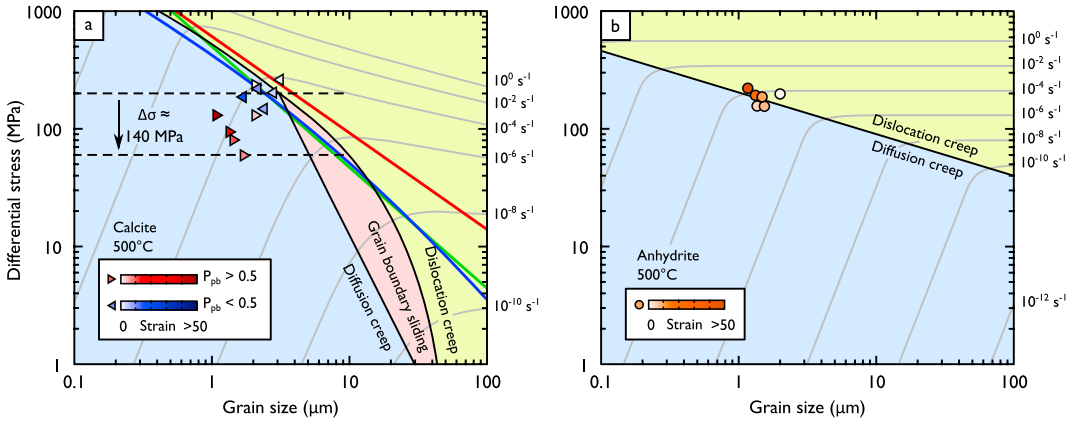


**Figure 10.** Deformation mechanism maps for (a) calcite, constructed from the dislocation creep flow law of *Renner et al*. [2002], the grain boundary sliding flow law of *Walker et al*. [1990], and the diffusion creep flow law of *Herwegh et al*. [2003] and (b) anhydrite, constructed from the dislocation and diffusion creep flow laws of *Dell'Angelo and Olgaard* [1995]. The thick black lines indicate the deformation mechanism field boundaries. For calcite, the paleopiezometers of *Barnhoorn et al*. [2004], red line, and *Rutter* [1995], green line, are given alongside the paleowattmeter of *Austin and Evans* [2007], blue line. Data points (colored by shear strain) are plotted using median grain-sizes (Figure 7c and Table S1) and the shear strain rates given in Table 1, converted to effective strain rates using a factor of $1/\sqrt{3}$ [*Paterson and Olgaard*, 2000].

monolayers form rather than the higher strains required for monolayer disaggregation and grain-scale phase mixing. The data points in Figure 10—assuming constant strain rate conditions—imply a stress drop in calcite of up to 140 MPa, or relative weakening of up to 60%, as a result of grain boundary pinning and the transition to diffusion creep. Anhydrite grain-sizes, on the other hand, plot entirely within the field boundary region, regardless of shear strain (Figure 10b) such that, at high strains, anhydrite is apparently stronger than calcite.

These findings are somewhat at odds with those of *Barnhoorn et al*. [2005] who, in similar calcite-anhydrite experiments, proposed that calcite remained in the dislocation creep regime at high strains ($\gamma > 5$), while anhydrite deformed by diffusion creep. In part, these inferences were based on the presence of elongate ribbons of calcite and small, equant grains of anhydrite. However, their microstructures are remarkably similar to ours, and we suggest that the elongate calcite ribbons observed in their BSE images are, in fact, highly sheared polycrystalline domains, composed also of small, equant grains. On the basis of grain shape and size alone, it could therefore be argued that in both this study and that of *Barnhoorn et al*. [2005], calcite and anhydrite are both deforming by GSS mechanisms.

*Barnhoorn et al*. [2005] also inferred deformation mechanisms by comparison to the end-member rheological data. They found that 100 vol % anhydrite aggregates deformed by diffusion creep ($n = 1$) at high strains [c.f. *Dell'Angelo and Olgaard*, 1995; *Bruhn and Casey*, 1997; *Bruhn et al*., 1999; *Heidelbach et al*., 2001; *Hildyard et al*., 2011], whereas 100 vol % calcite aggregates deformed by dislocation creep ($n = 4.2$). Admittedly, this contradicts the findings of our flow law analysis; however, the end-member rheologies are not necessarily indicative of two-phase rheology. Indeed, the homogeneity of the deformation in our experiments, and the ability of both phases to form long, thin layers, suggests that calcite and anhydrite are close to isoviscous at high strains in our experiments [*Handy*, 1990].

### 4.3. Strains Required for Geometric Phase Mixing

In our experiments, single-phase domains are progressively sheared to form thin monolayers that ultimately disaggregate at high strains to produce a fully homogeneous, mixed microstructure. The spatial density of interphase boundaries increases as domains are sheared and reaches a maximum when monolayers disaggregate into individual grains. As phase boundary density increases, the degree of grain boundary pinning also increases and, at a point, reaches a sufficient level to allow a transition to the strain-weakening GSS regime via grain-size reduction beyond the recrystallized grain-size piezometer. Our microstructural analyses indicate that this transition coincides with the formation of monolayers at $\gamma \sim 6$, since all grains within a

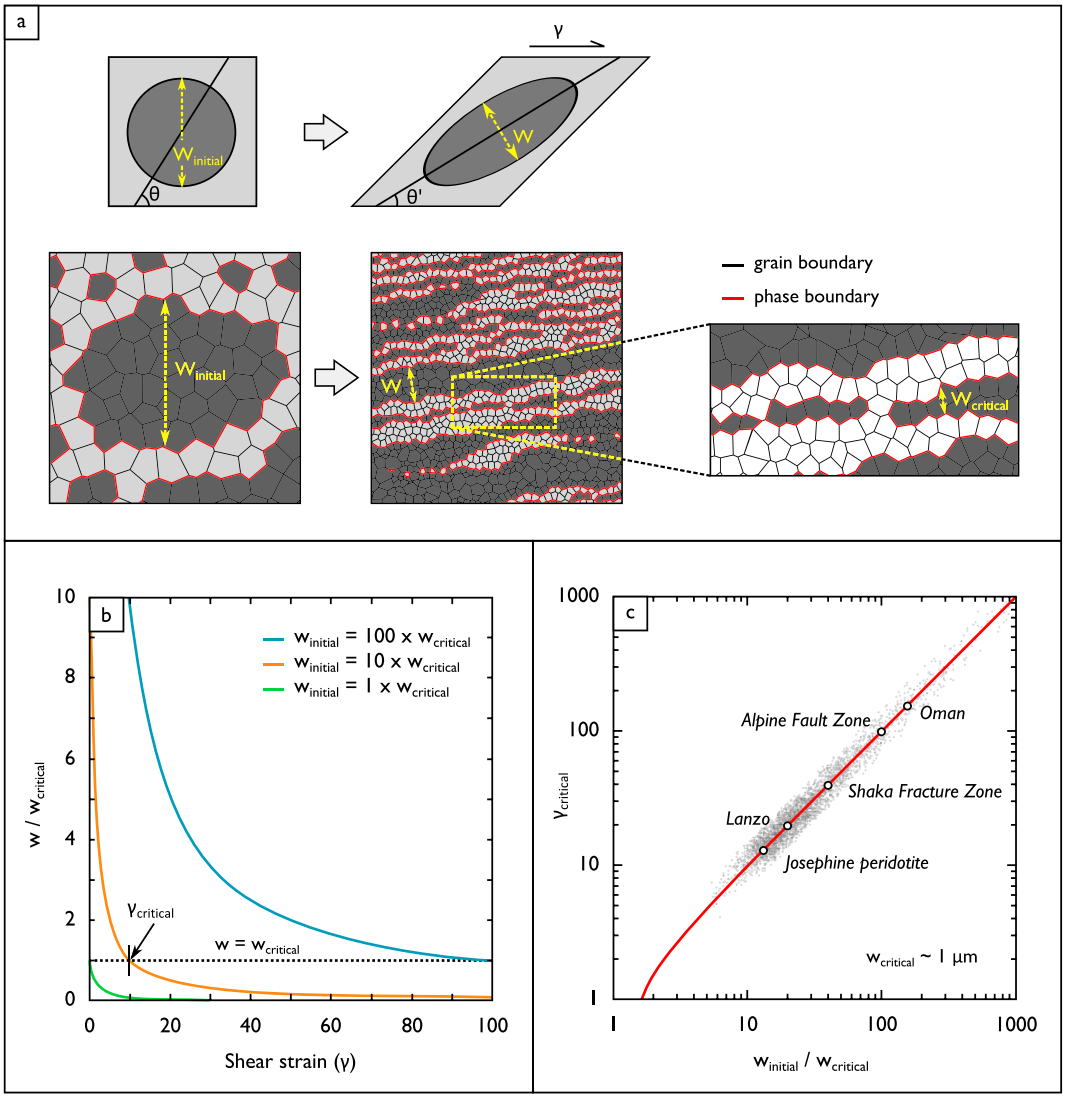


**Figure 11.** (a) The critical amount of strain, $\gamma_{critical}$, required to reach a monolayer state can be calculated using equations for the change in shape of the finite strain ellipse. (b, c) $\gamma_{critical}$ is dependent on the initial width of phase domains, $w_{initial}$, and the width of monolayers at which phase mixing is sufficient enough to allow rheological weakening, $w_{critical}$. The grey shaded symbols are derived from initial domain widths ($w_{initial}$) for our starting material, calculated from micro-CT data. Artificial noise (jitter) has been applied to the data to better illustrate the distribution. For reference, a few $w_{initial}/w_{critical}$ values are shown for natural ductile shear zones: the Oman and Lanzo peridotites [*Linckens et al.*, 2015], the Josephine peridotites [*Skemer et al.*, 2010], the Alpine Fault Zone [*Toy*, 2008], and the Shaka Fracture Zone [*Warren and Hirth*, 2006].

monolayer are in contact with phase boundary and therefore experience grain boundary pinning. Phase boundary density at $\gamma = 6$ is roughly 50% of that in the fully mixed sample (Figure 7b).

The critical shear strain, $\gamma_{critical}$, required to reach a monolayer state can be estimated from the equations of *Ramsay* [1980], which describe changes in the shape of the finite strain ellipse as function of shear strain

$$w = \left[\frac{1}{2}\left[2 + \gamma^2 - \gamma\left(\gamma^2 + 4\right)^{\frac{1}{2}}\right]\right]^{\frac{1}{2}} \quad (3)$$

where $w$ is the minor axis of the strain ellipse or, in this case, the domain width (Figure 11a). As shown in Figure 11b, the amount of strain required to reach a monolayer state ($w = w_{critical}$) is dependent on the initial size of the phase domains ($w_{initial}$): larger domains require more strain to reach a given critical width. As it turns out, there is almost a perfect 1:1 relationship between $w_{initial}/w_{critical}$ and $\gamma_{critical}$ (Figure 11c); in other

words, a shear strain of 10 is required to form monolayers from domains which are initially 10 times larger than $w_{critical}$ (the monolayer width).

Monolayers in our experiments are typically ~1 μm wide (Figure 6), while calcite domain widths, determined from micro-CT with a resolution limit of nominally 10 μm, are mostly between 12 μm (10th percentile) and 48 μm (90th percentile) in the starting material (Figure 2). Hence, in our experiments, a shear strain of 12 is estimated for the onset of monolayer formation and rheological weakening, and almost all domains should have formed monolayers by a shear strain of 48. This is, broadly speaking, consistent with our experimental observations: some large calcite domains are retained at $\gamma = 17$ but are all destroyed by $\gamma = 57$. However, the shear strain required for the onset of monolayer formation in our experiments is slightly less than that given above (roughly $\gamma = 6$; Figure 5d), specifically for domains of less than 12 μm width in the starting material (see Figure 5a).

In nature, shear zone protoliths have grain-sizes that are commonly ~100 times larger than grain-sizes in adjacent ultramylonites (e.g., Figures 1 and 11c). Thus, it is implied that shear strains up to, and perhaps in excess of 100 may be required for the onset of monolayer formation and associated rheological weakening, if mixing is by mechanical means only. This should, however, be considered an upper limit, since in many phase systems (olivine-orthopyroxene, for example), phase mixing may be aided by chemical reaction [e.g., *Newman et al*., 1999; *Kruse and Stünitz*, 1999; *Dijkstra et al*., 2002; *Kenkmann and Dresen*, 2002; *Hidas et al*., 2016]. As an example, in experiments on anorthite-diopside composites, *Dimanov et al*. [2007] reported extensive phase mixing at a shear strain of 5, which they attributed to grain boundary sliding, cavitation, and diffusion. It is also important to note that *complete* phase mixing is likely not necessary for rheological weakening, which requires only that a pervasive weak network of grains is formed [*Handy*, 1990]. Nonetheless, it is clear that shear zone formation involves a protracted stage of non-steady state microstructural and mechanical evolution.

## 5. Summary and Closing Remarks

Calcite-anhydrite composites were deformed to large shear strains to understand the underlying physical mechanisms of phase mixing: a process often proposed to enable strain localization in ductile shear zones. With increasing deformation, we observe a geometrically-driven thinning and stretching of domains of both calcite and anhydrite, ultimately leading to the formation of finely laminated monolayers of one grain's width. Monolayer formation begins at a shear strain of ~6 and drives an increase in the spatial density of interphase boundaries, enhancing grain boundary pinning. Grain boundary pinning suppresses grain growth and enables grains to reduce in size beyond the theoretical lower limit of grain-size established by the recrystallized grain-size piezometer or dislocation-diffusion creep boundary. Rheological weakening related to a transition to diffusion-dominated creep is predicted to coincide with monolayer formation at a shear strain of ~6, since all grains within monolayers are in contact with phase boundaries, and therefore become pinned. Monolayers ultimately disaggregate at high strains ($17 < \gamma < 57$) to form a homogenous, fully mixed microstructure that, in these experiments, may be up to 60% weaker than the starting material. This geometric phase mixing mechanism is entirely mechanical and does not depend on cavitation, diffusion, or reaction. A model for the geometric thinning and stretching of domains during simple shear shows that an approximate 1:1 relationship exists between the strains required to form monolayers and the ratio of the starting domain width to the monolayer width. The model demonstrates that rheological weakening associated with the formation of monolayers may require large strains in nature ($\gamma \leq 100$), since protolith grains are often up to 100 times larger than grains in adjacent ultramylonites.

The microstructures observed here are remarkably similar to those documented in natural ductile shear zones [e.g., *Kruse and Stünitz*, 1999; *Kenkmann and Dresen*, 2002; *Mehl and Hirth*, 2008; *Linckens et al*., 2015], where thin layers (i.e., foliation) formed during mylonitization were observed to separate into individual grains at around the mylonite-ultramylonite boundary (e.g., Figure 1). Our experiments demonstrate that large strains ($\gamma \leq 100$) may be required for rheological weakening caused by the formation of thin compositional layering, particularly where protolith domain/grain-sizes are large. However, the large strains required for geometric phase mixing should be considered an upper bound on the strain scales required for rheological weakening due to phase mixing. Contributions to phase mixing from diffusion and petrologic reactions will both serve to make phase mixing more efficient. Nonetheless, the long transient interval between the

initiation of localized deformation and the formation of ultramylonitic textures in nature suggests that other mechanisms must be required to initiate shear localization [*Skemer et al*., 2013]. Ultramylonite formation is therefore a consequence, not the cause, of shear localization but, regardless, is essential to the preservation of weak zones and the formation of Earth-like plate boundaries in the crust and upper mantle.

**Acknowledgments**
We thank Hélène Couvy for helpful discussions and for her assistance developing the LVT cell assembly used in this study. Jolien Linckens is thanked for providing us with the photomicrographs shown in Figure 1. We are also grateful to Auke Barnhoorn for providing samples from his work to compare with our own. Mike Sly provided the EBSD data for undeformed Carrara marble. Georg Dresen and Elena Miranda provided constructive reviews that significantly improved the clarity of the manuscript. This work was funded by NSF grants EAR-1360584 and EAR-1352306, and support from the Washington University Institute of Materials Science and Engineering was awarded to P.S. and additional funding from the McDonnell Center for the Space Sciences for A.J.C. All data presented in this study can be obtained from the corresponding author upon request.

## References

Austin, N., and B. Evans (2009), The kinetics of microstructural evolution during deformation of calcite, *J. Geophys. Res.*, *114*, B09402, doi:10.1029/2008JB006138.
Austin, N. J., and B. Evans (2007), Paleowattmeters: A scaling relation for dynamically recrystallized grain-size, *Geology*, *35*(4), 343–346.
Bachmann, F., R. Hielscher, and H. Schaeben (2010), Texture analysis with MTEX–free and open source software toolbox, in *Solid State Phenomena*, vol. 160, pp. 63–68, Trans Tech Publ., Switzerland.
Barnhoorn, A., M. Bystricky, L. Burlini, and K. Kunze (2004), The role of recrystallisation on the deformation behaviour of calcite rocks: Large strain torsion experiments on Carrara marble, *J. Struct. Geol.*, *26*(5), 885–903.
Barnhoorn, A., M. Bystricky, K. Kunze, L. Burlini, and J. P. Burg (2005), Strain localisation in bimineralic rocks: Experimental deformation of synthetic calcite-anhydrite aggregates, *Earth Planet. Sci. Lett.*, *240*(3), 748–763.
Bercovici, D. (2003), The generation of plate tectonics from mantle convection, *Earth Planet. Sci. Lett.*, *205*(3), 107–121.
Bercovici, D., and Y. Ricard (2012), Mechanisms for the generation of plate tectonics by two-phase grain-damage and pinning, *Phys. Earth Planet. Inter.*, *202*, 27–55.
Bercovici, D., and Y. Ricard (2016), Grain-damage hysteresis and plate tectonic states, *Phys. Earth Planet. Inter.*, *253*, 31–47.
Bestmann, M., and D. J. Prior (2003), Intragranular dynamic recrystallization in naturally deformed calcite marble: Diffusion accommodated grain boundary sliding as a result of subgrain rotation recrystallization, *J. Struct. Geol.*, *25*(10), 1597–1613.
Brace, W. F., and D. L. Kohlstedt (1980), Limits on lithospheric stress imposed by laboratory experiments, *J. Geophys. Res.*, *85*(B11), 6248–6252, doi:10.1029/JB085iB11p06248.
Bridgman, P. W. (1940), The Measurement of Hydrostatic Pressure to 30,000 kg/cm$^2$, in *Proceedings of the American Academy of Arts and Sciences*, vol. 74, pp. 1–10, American Academy of Arts & Sciences, Cambridge, Mass.
Bruhn, D. F., and M. Casey (1997), Texture development in experimentally deformed two-phase aggregates of calcite and anhydrite, *J. Struct. Geol.*, *19*(7), 909–925.
Bruhn, D. F., D. L. Olgaard, and L. N. Dell'Angelo (1999), Evidence for enhanced deformation in two-phase rocks: Experiments on the rheology of calcite-anhydrite aggregates, *J. Geophys. Res.*, *104*(B1), 707–724, doi:10.1029/98JB02847.
Chen, I. W. (1982), Diffusional creep of two-phase materials, *Acta Metall.*, *30*(8), 1655–1664.
Cross, A. J., S. Ellis, and D. J. Prior (2015), A phenomenological numerical approach for investigating grain-size evolution in ductiley deforming rocks, *J. Struct. Geol.*, *76*, 22–34.
De Bresser, J., J. Ter Heege, and C. Spiers (2001), Grain-size reduction by dynamic recrystallization: Can it result in major rheological weakening?, *Int. J. Earth Sci.*, *90*(1), 28–45.
Dell'Angelo, L. N., and D. L. Olgaard (1995), Experimental deformation of fine-grained anhydrite: Evidence for dislocation and diffusion creep, *J. Geophys. Res.*, *100*(B8), 15,425–15,440, doi:10.1029/95JB00956.
Dijkstra, A. H., M. R. Drury, R. L. Vissers, and J. Newman (2002), On the role of melt-rock reaction in mantle shear zone formation in the Othris Peridotite Massif (Greece), *J. Struct. Geol.*, *24*(9), 1431–1450.
Dimanov, A., E. Rybacki, R. Wirth, and G. Dresen (2007), Creep and strain-dependent microstructures of synthetic anorthite–diopside aggregates, *J. Struct. Geol.*, *29*(6), 1049–1069.
Doube, M., M. M. Kłosowski, I. Arganda-Carreras, F. P. Cordelières, R. P. Dougherty, J. S. Jackson, B. Schmid, J. R. Hutchinson, and S. J. Shefelbine (2010), BoneJ: Free and extensible bone image analysis in ImageJ, *Bone*, *47*(6), 1076–1079.
Drury, M. R., H. A. Lallemant, G. M. Pennock, and L. N. Palasse (2011), Crystal preferred orientation in peridotite ultramylonites deformed by grain-size sensitive creep, Étang de Lers, Pyrenees, France, *J. Struct. Geol.*, *33*(12), 1776–1789.
Evans, B., J. Renner, and G. Hirth (2001), A few remarks on the kinetics of static grain growth in rocks, *Int. J. Earth Sci.*, *90*(1), 88–103.
Farla, R. J., S. I. Karato, and Z. Cai (2013), Role of orthopyroxene in rheological weakening of the lithosphere via dynamic recrystallization, *Proc. Natl. Acad. Sci. U.S.A.*, *110*(41), 16,355–16,360.
Fusseis, F., K. Regenauer-Lieb, J. Liu, R. M. Hough, and F. De Carlo (2009), Creep cavitation can establish a dynamic granular fluid pump in ductile shear zones, *Nature*, *459*(7249), 974–977.
Handy, M. R. (1990), The solid-state flow of polymineralic rocks, *J. Geophys. Res.*, *95*(B6), 8647–8661, doi:10.1029/JB095iB06p08647.
Heidelbach, F., I. C. Stretton, and K. Kunze (2001), Texture development of polycrystalline anhydrite experimentally deformed in torsion, *Int. J. Earth Sci.*, *90*(1), 118–126.
Herwegh, M., X. Xiao, and B. Evans (2003), The effect of dissolved magnesium on diffusion creep in calcite, *Earth Planet. Sci. Lett.*, *212*(3), 457–470.
Hidas, K., A. Tommasi, C. J. Garrido, J. A. Padrón-Navarta, D. Mainprice, A. Vauchez, F. Barou, and C. Marchesi (2016), Fluid-assisted strain localization in the shallow subcontinental lithospheric mantle, *Lithos*, *262*, 636–650.
Hildyard, R. C., D. J. Prior, E. Mariani, and D. R. Faulkner (2009), Crystallographic preferred orientation (CPO) of gypsum measured by electron backscatter diffraction (EBSD), *J. Microsc.*, *236*(3), 159–164.
Hildyard, R. C., D. J. Prior, E. Mariani, and D. R. Faulkner (2011), Characterization of microstructures and interpretation of flow mechanisms in naturally deformed, fine-grained anhydrite by means of EBSD analysis, *Geol. Soc. London, Spec. Publ.*, *360*(1), 237–255.
Kenkmann, T., and G. Dresen (2002), Dislocation microstructure and phase distribution in a lower crustal shear zone–an example from the Ivrea-Zone, Italy, *Int. J. Earth Sci.*, *91*(3), 445–458.
Kilian, R., R. Heilbronner, and H. Stünitz (2011), Quartz grain-size reduction in a granitoid rock and the transition from dislocation to diffusion creep, *J. Struct. Geol.*, *33*(8), 1265–1284.
Kruse, R., and H. Stünitz (1999), Deformation mechanisms and phase distribution in mafic high-temperature mylonites from the Jotun Nappe, southern Norway, *Tectonophysics*, *303*(1), 223–249.
Linckens, J., M. Herwegh, O. Müntener, and I. Mercolli (2011), Evolution of a polymineralic mantle shear zone and the role of second phases in the localization of deformation, *J. Geophys. Res.*, *116*, B06210, doi:10.1029/2010JB008119.
Linckens, J., R. H. Bruijn, and P. Skemer (2014), Dynamic recrystallization and phase mixing in experimentally deformed peridotite, *Earth Planet. Sci. Lett.*, *388*, 134–142.

Linckens, J., M. Herwegh, and O. Müntener (2015), Small quantity but large effect—How minor phases control strain localization in upper mantle shear zones, *Tectonophysics*, *643*, 26–43.
Mehl, L., and G. Hirth (2008), Plagioclase preferred orientation in layered mylonites: Evaluation of flow laws for the lower crust, *J. Geophys. Res.*, *113*, B05202, doi:10.1029/2007JB005075.
Menegon, L., F. Fusseis, H. Stünitz, and X. Xiao (2015), Creep cavitation bands control porosity and fluid flow in lower crustal shear zones, *Geology*, *43*(3), 227–230.
Miranda, E. A., G. Hirth, and B. E. John (2016), Microstructural evidence for the transition from dislocation creep to dislocation-accommodated grain boundary sliding in naturally deformed plagioclase, *J. Struct. Geol.*, *92*, 30–45.
Montési, L. G. (2013), Fabric development as the key for forming ductile shear zones and enabling plate tectonics, *J. Struct. Geol.*, *50*, 254–266.
Newman, J., W. M. Lamb, M. R. Drury, and R. L. Vissers (1999), Deformation processes in a peridotite shear zone: Reaction-softening by an H 2 O-deficient, continuous net transfer reaction, *Tectonophysics*, *303*(1), 193–222.
Okudaira, T., and N. Shigematsu (2012), Estimates of stress and strain rate in mylonites based on the boundary between the fields of grain-size sensitive and insensitive creep, *J. Geophys. Res.*, *117*, B03210, doi:10.1029/2011JB008799.
Olgaard, D. L. (1990), The role of second phase in localizing deformation, *Geol. Soc. London, Spec. Publ.*, *54*(1), 175–181.
Passchier, C. W., and R. A. J. Trouw (2005), *Microtectonics*, 2nd ed., Springer, Berlin.
Paterson, M. S., and D. L. Olgaard (2000), Rock deformation tests to large shear strains in torsion, *J. Struct. Geol.*, *22*(9), 1341–1358.
Pearce, M. A. (2015), EBSDinterp 1.0: A MATLAB® Program to Perform Microstructurally Constrained Interpolation of EBSD Data, *Microsc. Microanal.*, *21*(04), 985–993.
Pearce, M. A., and J. Wheeler (2011), Grain growth and the lifetime of diffusion creep deformation, *Geol. Soc. London, Spec. Publ.*, *360*(1), 257–272.
Platt, J. P. (2015), Rheology of two-phase systems: A microphysical and observational approach, *J. Struct. Geol.*, *77*, 213–227.
Rahl, J. M., and P. Skemer (2016), Microstructural evolution and rheology of quartz in a mid-crustal shear zone, *Tectonophysics*, *680*, 129–139.
Ramsay, J. G. (1980), Shear zone geometry: A review, *J. Struct. Geol.*, *2*(1), 83–99.
Renner, J., Evans, B., and Siddiqi, G. (2002), Dislocation creep of calcite, *J. Geophys. Res.*, *107*(B12), 2364, doi:10.1029/2001JB001680.
Rutter, E. H. (1995), Experimental study of the influence of stress, temperature, and strain on the dynamic recrystallization of Carrara marble, *J. Geophys. Res.*, *100*(B12), 24,651–24,663, doi:10.1029/95JB02500.
Rybacki, E., R. Wirth, and G. Dresen (2008), High-strain creep of feldspar rocks: Implications for cavitation and ductile failure in the lower crust, *Geophys. Res. Lett.*, *35*, L04304, doi:10.1029/2007GL032478.
Skemer, P., and S. I. Karato (2008), Sheared lherzolite xenoliths revisited, *J. Geophys. Res.*, *113*, B07205, doi:10.1029/2007JB005286.
Skemer, P., I. Katayama, Z. Jiang, and S. I. Karato (2005), The misorientation index: Development of a new method for calculating the strength of lattice-preferred orientation, *Tectonophysics*, *411*(1), 157–167.
Skemer, P., J. M. Warren, and P. B. Kelemen (2010), Microstructural and rheological evolution of a mantle shear zone, *J. Petrol.*, *51*(1–2), 43–53.
Skemer, P., J. M. Warren, L. N. Hansen, G. Hirth, and P. B. Kelemen (2013), The influence of water and LPO on the initiation and evolution of mantle shear zones, *Earth Planet. Sci. Lett.*, *375*, 222–233.
Smith, C. S. (1948), Grains, phases, and interfaces: An interpretation of microstructure, *Trans. Am. Inst. Mining Metall. Eng.*, *175*, 15–51.
Sundberg, M., and R. F. Cooper (2008), Crystallographic preferred orientation produced by diffusional creep of harzburgite: Effects of chemical interactions among phases during plastic flow, *J. Geophys. Res.*, *113*, B12208, doi:10.1029/2008JB005618.
Tackley, P. J. (1998), Self-consistent generation of tectonic plates in three-dimensional mantle convection, *Earth Planet. Sci. Lett.*, *157*(1), 9–22.
Toy, V. (2008), Rheology of the Alpine Fault mylonite zone: Deformation processes at and below the base of the seismogenic zone in a major plate boundary structure (Doctoral dissertation, University of Otago).
Vissers, R. L. M., M. R. Drury, E. H. Hoogerduijn, C. J. Spiers, and D. Van der Wal (1995), Mantle shear zones and their effect on lithosphere strength during continental breakup, *Tectonophysics*, *249*(3), 155–171.
Walker, A. N., E. H. Rutter, and K. H. Brodie (1990), Experimental study of grain-size sensitive flow of synthetic, hot-pressed calcite rocks, *Geol. Soc. Lond. Spec. Publ.*, *54*(1), 259–284.
Warren, J. M., and G. Hirth (2006), Grain-size sensitive deformation mechanisms in naturally deformed peridotites, *Earth Planet. Sci. Lett.*, *248*(1), 438–450.
Wheeler, J. (1992), Importance of pressure solution and Coble creep in the deformation of polymineralic rocks, *J. Geophys. Res.*, *97*(B4), 4579–4586, doi:10.1029/91JB02476.
Wheeler, J. (2009), The preservation of seismic anisotropy in the Earth's mantle during diffusion creep, *Geophys. J. Int.*, *178*(3), 1723–1732.
Zhang, Y., B. E. Hobbs, and M. W. Jessell (1994), The effect of grain-boundary sliding on fabric development in polycrystalline aggregates, *J. Struct. Geol.*, *16*(9), 1315–1325.